

SCIENTIFIC REPORTS

OPEN

Dependence of Solidification for $\text{Bi}_2\text{Te}_{3-x}\text{Se}_x$ Alloys on Their Liquid States

Yuan Yu^{1,2}, Zhan Wu¹, Oana Cojocaru-Miréidin², Bin Zhu¹, Xiao-Yu Wang¹, Na Gao¹, Zhong-Yue Huang¹ & Fang-Qiu Zu¹

The resistivity *versus* temperature (ρ - T) behaviours of liquid n-type $\text{Bi}_2\text{Te}_{3-x}\text{Se}_x$ ($x = 0.3, 0.45$ and 0.6) alloys are explored up to 1050°C . A clear hump is observed on all ρ - T curves of the three studied $\text{Bi}_2\text{Te}_{3-x}\text{Se}_x$ melts during the heating process, which suggests that a temperature-induced liquid-liquid structural transition takes place in the melts. Based on this information, the solidification behaviours and microstructures of the alloys with different liquid states are investigated. The samples that experienced liquid structural transition show that the nucleation and growth undercooling degrees are conspicuously enlarged and the solidification time is shortened. As a result, the solidified lamellae are refined and homogenized, the prevalence of low-angle grain boundaries between these lamellae is increased, and the Vicker Hardness is enhanced. Atom probe tomography analyses prove that there is no segregation or nanoprecipitation within the grains, but the Te-rich eutectic structure and the evolution of composition near the Te-matrix phase boundary are investigated in a sample that experienced liquid structural transition. Our work implies that the solidification behaviours of $\text{Bi}_2\text{Te}_{3-x}\text{Se}_x$ alloys are strongly related to their parent liquid states, providing an alternative approach to tailor the thermoelectric and mechanical properties even when only a simple solidification process is performed.

With the increasing concern of environmental pollution and energy crisis, thermoelectric (TE) materials, which can directly interconvert electrical energy and thermal energy, have received considerable attentions^{1,2}. Bi_2Te_3 -based solid solutions, including $(\text{Bi}, \text{Sb})_2\text{Te}_3$ and $\text{Bi}_2(\text{Te}, \text{Se})_3$, are known as the best thermoelectric materials at temperatures from 300 K to 500 K ^{3,4}. In addition, these alloys also exhibit outstanding properties as phase change materials⁵ and topological insulators⁶. The commercial Bi_2Te_3 -based TE legs are generally prepared by unidirectional solidification methods, such as zone melting⁷, Bridgman⁸, and Czochralski⁹. Peak TE figure of merit values of these melt-grown ingots are typically in the range of 0.8 to 1.1 along the preferentially oriented ab-plane^{4,10}. However, the lamellar structure and weak van der Waals bond between the Te-Te layers make them susceptible to cleavage along this basal plane, imparting very poor mechanical properties, and hence limiting their application potentials¹⁰. To improve the TE performance and mechanical properties of Bi_2Te_3 -based compounds, various alternative processing techniques have been widely implemented, such as ball milling or melt spinning plus powder sintering^{11,12}, hot deformation¹³, and high-pressure fabrication¹⁴. Although these methods have been shown efficient to improve the thermoelectric properties, the relatively high energy consumption, low production efficiency, and relatively sophisticated equipment required for production processes cannot be overlooked. Therefore, it is worthwhile to attempt to synthesize bulk TE materials with satisfactory microstructures and properties via a free solidification method.

There has been a notable trend in engineering practices that the properties and solidified microstructures of many alloys are dependent on the thermal history of their parent liquids^{15–18}. Both theoretical and experimental results suggest that the liquid structures and their properties might be discontinuously changed as a function of pressure or temperature^{19–21}. Thus, the alteration of the solidification microstructures due to different thermal histories may be ascribed to their different liquid states. Hitherto, the temperature-induced liquid-liquid structural transition (TL-LLST) has been suggested to occur in some single- and multiple-component melts, such as Bi-Te^{15,16}, Pb-Bi²²,

¹Liquid/Solid Metal Processing Institute, School of Materials Science & Engineering, Hefei University of Technology, Tunxi Road 193, Hefei, 230009, China. ²Physikalisches Institut (IA), Sommerfeldstraße 14, RWTH Aachen, 52074, Aachen, Germany. Correspondence and requests for materials should be addressed to F.-Q.Z. (email: fangqiuзу@hotmail.com) or Z.-Y.H. (email: zyhuang1981@hotmail.com)

Sample	x = 0.3 A ^a	x = 0.3 B ^b	x = 0.45 A	x = 0.45 B	x = 0.6 A	x = 0.6 B
Composition	Bi ₂ Te _{2.7} Se _{0.3}		Bi ₂ Te _{2.55} Se _{0.45}		Bi ₂ Te _{2.4} Se _{0.6}	
Transition ranges	790.6~900.4 °C		810.1~940.5 °C		800.7~920.6 °C	
Smelting process	750 °C; 1.5 h	900 °C; 1.5 h	750 °C; 1.5 h	1000 °C; 1.5 h	750 °C; 1.5 h	950 °C; 1.5 h
T – P ^c process	650 °C; 1 h (for all samples)					

Table 1. Specific sample smelting processes for Bi₂T_{3–x}Se_x (x = 0.3, 0.45, 0.6) alloys. These samples are used for investigating the solidification processes and corresponding microstructures and mechanical properties. ^aA represents smelted at temperatures below the range of TI-LLST. ^bB represents smelted at temperatures above the range of TI-LLST. ^cT – P represents temperature-preservation.

and Bi-Sb²³ by various reports. More significantly, changing the liquid states, based on the TI-LLST behaviour, has been confirmed to be effective in regulating the solidification processes and microstructures^{15–17, 22, 23}.

Our previous studies demonstrated the feasibility of changing the liquid state to modify the solidification microstructures and TE properties of p-type Bi₂Te_{3–x}-based alloys^{15, 16}. This motivates us to further explore the effect of TI-LLST on their n-type counterparts. Hence, in this work, the resistivity-temperature (ρ -T) behaviours of the n-type Bi₂Te_{3–x}Se_x (x = 0.3, 0.45, 0.6) liquid alloys were explored, the results of which suggested the occurrence of an irreversible TI-LLST during the first heating process. Moreover, after experiencing TI-LLST, the microstructures of the Bi₂Te_{3–x}Se_x alloys were effectively refined compared with those obtained from the conventional solidification conditions, which leads to the increased amount of low-angle grain boundaries and enhanced Vicker Hardness. Atom probe tomography (APT) analysis was carried out, to our best knowledge, for the first time on this kind of semiconductor. The results show that the solidified microstructures are very homogenous at the nanoscale without segregation or precipitation in the grain interior. Nevertheless, the Te-rich eutectic structure was investigated in the sample which experienced TI-LLST. The composition evolution near the interface between the Te-rich phase and the matrix at nanometre scale was also analysed by APT. It is believed that the interrelationship between the parent liquid states and the solidified microstructures uncovered by this work may help to better understand the solidification process of this kind of material. Furthermore, it provides a new control over the structural configuration of TE materials with possible relevance to improvement of their properties.

Methods

According to the stoichiometry of Bi₂T_{3–x}Se_x (x = 0.3, 0.45, 0.6) alloys, high purity (5 N) elemental granules of Bi, Te and Se were weighed and then melted at 650 °C for 3 hours under B₂O₃ flux protection. Subsequently, the melted samples were poured into quartz measuring cells to record the temperature-dependent liquid-state resistivity using the DC four-probe method in an electrical furnace at ramping and cooling speeds of 5 °C/min under high-purity Argon (5 N) atmosphere¹⁶. These samples were only used to investigate the liquid resistivity behaviours *versus* temperature. The same measurements were repeated three times, and the results were well reproducible.

To explore the relationship between solidification behaviour and different liquid states, six new samples were prepared. Smelting processes were carried out according to the anomalous humps on the ρ -T curves, as specified in Table 1. The smelting process at temperatures below the hump is a conventional one, which normally possesses an overheat degree of near 100 °C. Here, the high-temperature smelting process (at least 300 °C overheated) is designed to induce the potential TI-LLST to obtain distinct liquid states. In order to exclude the influence of solidification temperature field on the microstructures, all samples were maintained at 650 °C for 1 h after the smelting process and then air-cooled with crucibles and protective covers. The cooling processes were recorded utilizing a Keithley-2182 Nanovoltmeter with K-type thermocouples. Six cylindrical ingots were obtained after cooling. More experimental details can be found in our previous paper¹⁶.

Various techniques were utilized to characterize the structural and chemical properties of these as-cast ingots. The samples were polished and then etched in HCl-9% H₂O₂(L) for the optical microscopy observation. X-ray diffraction (XRD, D/MAX2500 V, Rigaku) was operated at 40 kV/40 mA using Cu – k_{α} radiation ($\lambda = 1.5406 \text{ \AA}$). Scanning electron microscopy (SEM) with energy dispersive spectrometer (EDS, Oxford) and electron back-scatter diffraction (EBSD, EDAX) were carried out on a SEM-FIB dual beam system (Helios 650, FEI). Atom probe tomography (APT) was utilized to investigate the three-dimensional (3D) elemental distribution at nanometre scale. The APT tips were prepared using the site-specific “lift-out” process in a SEM-FIB dual beam system (Helios 650) as schematically shown in Fig. 1. The APT tips were field evaporated in a local electrode atom probe (LEAP[®] 4000 X Si, Cameca) by applying a picosecond ultraviolet (UV) laser (wavelength = 355 nm). The experimental parameters for APT are as follows: base temperature of 50 K, laser pulse energy of 30 pJ, pulse repetition rate of 200 kHz, detection rate of 1%, flight length of 160 mm. The detector efficiency is about 50% due to the morphology of the microchannel plate (MCP). The APT data was analysed using IVAS 3.6.12TM. The Vicker Hardness measurement was conducted on a MH-3L equipment with a load of 0.245 N and holding time of 10 s. Ten data points were recorded for each sample.

Data Availability. The datasets generated during and/or analysed during the current study are available from the corresponding author on reasonable request.

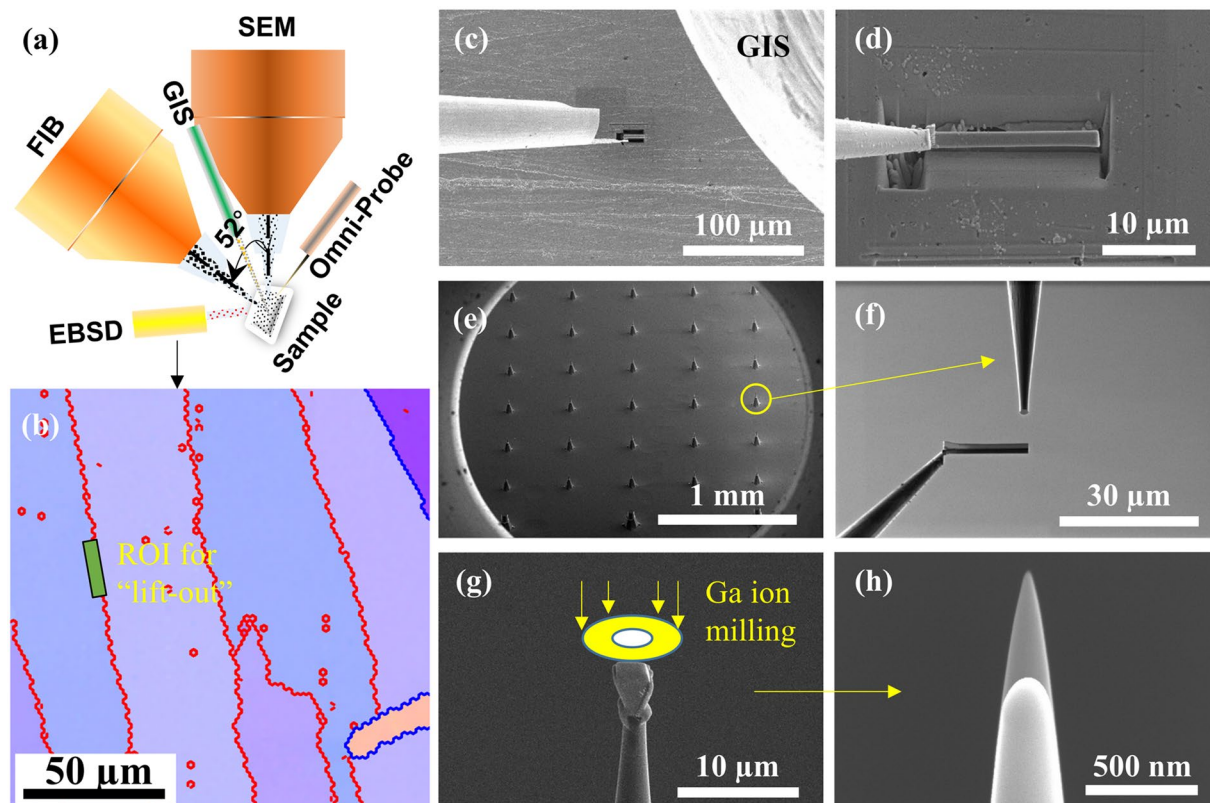


Figure 1. Site-specific “lift-out” process for preparing APT tips. **(a)** Schematic diagram of SEM-FIB dual beam system with EBSD attachment; **(b)** EBSD sample surface overlapped with grain boundaries. The green bar is the region of interest (ROI) for the “lift-out” process; **(c)** The micromanipulator (Omni-probe, left) and the gas injection system (GIS, right); **(d)** The Omni-probe and the ROI of sample are welded with Pt; **(e)** Microtip™ array coupon with 36 Si post; **(f)** Enlarged view of Si post and the sample before mounting on it; **(g)** One tip before suffering the Ga ion annular milling; **(h)** The APT tip profiles before (longer) and after (shorter) the measurement with tip radius of near 50 nm and 130 nm, respectively.

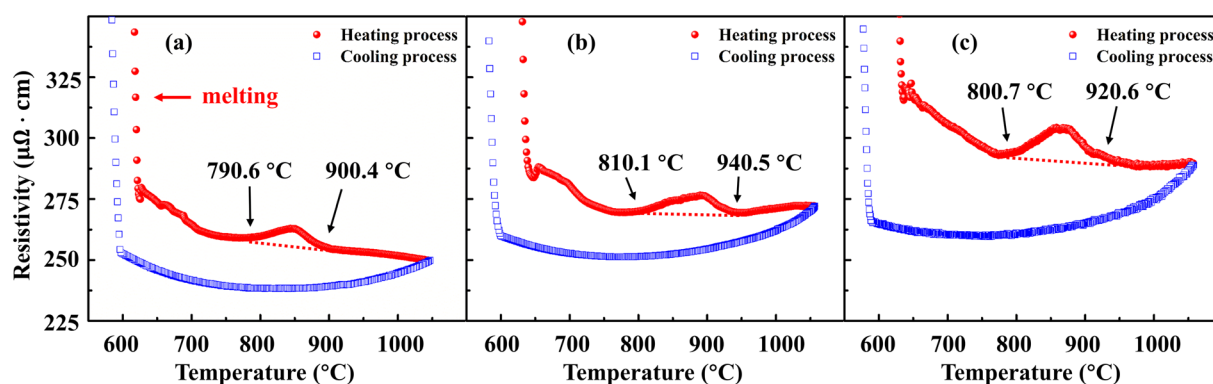


Figure 2. The ρ - T curves of liquid $\text{Bi}_2\text{Te}_{3-x}\text{Se}_x$ alloys during heating and cooling processes (5 °C/min). **(a)** $x = 0.3$; **(b)** $x = 0.45$; **(c)** $x = 0.6$.

Results and Discussion

The plots of electrical resistivity (ρ) of $\text{Bi}_2\text{Te}_{3-x}\text{Se}_x$ ($x = 0.3, 0.45, 0.6$) liquid alloys as a function of temperature during heating and cooling processes are shown in Fig. 2. During melting the electrical resistivity decreases abruptly, which can be attributed to the alloys' semiconductor character²⁴. After melting, the ρ - T curves of liquid alloys show a nonlinear relationship, which is different from the behaviour of metals²⁴. As the temperature further increases, intriguingly, an anomalous hump arises on the ρ - T curves of liquid $\text{Bi}_2\text{Te}_{2.7}\text{Se}_{0.3}$, $\text{Bi}_2\text{Te}_{2.55}\text{Se}_{0.45}$, and $\text{Bi}_2\text{Te}_{2.4}\text{Se}_{0.6}$ within 790.6–900.4 °C, 810.1–940.5 °C, and 800.7–920.6 °C during the heating process, respectively. However, the resistivity curves become smooth in the subsequent cooling processes, which suggests that

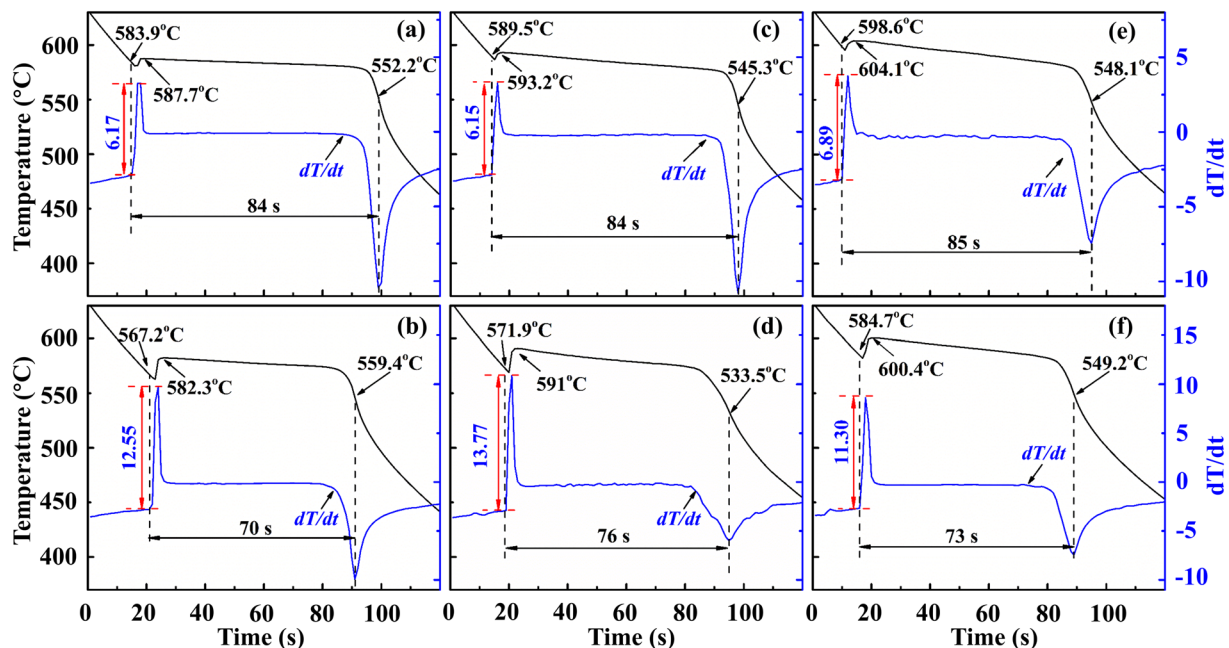


Figure 3. Cooling curves for $\text{Bi}_2\text{Te}_{3-x}\text{Se}_x$ liquid alloys. The temperature indicated by the first arrow from the left side of each picture is the nucleation temperature, T_N . The second arrow indicates the recrystallization temperature, T_G . The red double sided arrow shows the height of the first peak for dT/dt curve, Δh . The black double sided arrow shows the solidification time. (a) $x = 0.3$ -A; (b) $x = 0.3$ -B; (c) $x = 0.45$ -A; (d) $x = 0.45$ -B; (e) $x = 0.6$ -A; (f) $x = 0.6$ -B.

the liquid state change is irreversible. The physical mechanism of this anomalous hump on the ρ - T curve was discussed in our previous work^{15, 16, 25}. This abnormal phenomenon is well reproducible in several repeated experiments. The similar phenomena were also observed in pure Bi and Bi- and Sb-based melts and cross verified by DSC, DTA, internal friction, and XRD methods^{22, 26, 27}. Since the electrical resistivity is structure sensitive according to the generalized Faber-Ziman theory²⁸, the anomalous phenomena on the ρ - T curves allude to the occurrence of an irreversible TI-LLST in the $\text{Bi}_2\text{Te}_{3-x}\text{Se}_x$ liquid alloys.

According to the resistivity anomaly temperatures, the melting and solidification experiments on $\text{Bi}_2\text{Te}_{3-x}\text{Se}_x$ alloys in different liquid states were carried out as described in the experimental part. The cooling curves of all samples were recorded for exploring the solidification behaviour during the solidification process. The characteristic solidification parameters were calculated by the Newton thermal analysis method²⁹. Figure 3 shows that the cooling curve mainly evolves along four steps. The fast decline, in the beginning, corresponds to the liquid cooling process with a near constant cooling rate as implied by the first plateau of the first-order differentiation (dT/dt) curve. After that, the liquid alloy starts to largely nucleate and release the solidification latent heat, leading to the abrupt ascent of the dT/dt curve. The maximum value of dT/dt is related to the recrystallization temperature, which is also the crystal growth temperature (T_G). During the crystal growth process, both liquid and solid states coexist. Finally, when all liquid phases transform into solid states, the solidified ingot cools down very fast (abrupt decline of the dT/dt curve) in the ambient condition. The calculated results from the cooling curves, as shown in Fig. 3 and Supplementary Table S1, demonstrate that the characteristic solidification parameters for alloys solidified from distinct liquid states are quite different. Obviously, the nucleation temperature (T_N) of the B-group specimens (with TI-LLST) is significantly lower than that of the A-group specimens (without TI-LLST), which means that the solidification undercooling degree for B-group specimens is larger. The height of the first peak (Δh) for dT/dt curve of the B-group specimens is markedly larger than that of the A-group specimens, which is believed to arise from the larger nucleation rate. During the crystal growth stage, the T_G of B-group specimens is lower than that of their comparative counterparts, and the crystal growth time of the B-group specimens is also significantly shortened. The decreased crystal growth time, on the one hand, comes from the larger nucleation rate and more homogeneously distributed nuclei, and on the other hand, is on account of the lower growth temperature which provides larger growth driving force³⁰. In the following context, we offer an explanation of the observation that the two sets of samples present distinguishable solidification behaviours and microstructures.

As is well known, the liquid structures at temperatures not far above liquidus are normally inhomogeneous, containing solid-like, topologically short-range ordered and/or chemically short-range ordered clusters²⁰. These clusters dissipate and engender new ones, but they do not vanish; they have statistical structures, sizes, and constituents that change continuously with temperature. Additionally, it is more widely accepted that polymorphism exists in liquid states³¹, and critical points between stable liquids or/and metastable ones are revealed^{32, 33}. Mudry³⁴ reported that, not far from the liquidus, the structure of liquid Bi-Te alloys in the range of 52–60 at.% Te still possesses short-range ordered clusters that are similar to the solid structure of Bi_2Te_3 . Neutron diffraction studies also indicate that the crystalline Bi_2Se_3 -like configuration of Bi-Se pairs remains to some extent in the liquid state^{35, 36}.

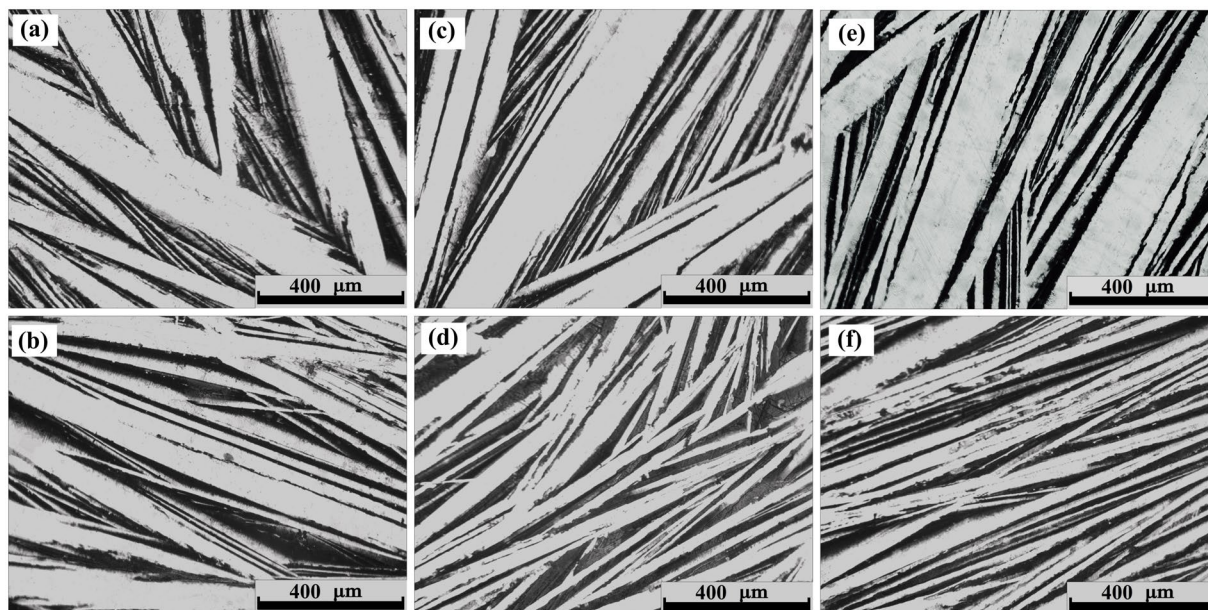


Figure 4. Solidification microstructures as observed by optical microscopy along the radial direction of the cylindrical ingot for both A-group (upper row) and B-group (lower row) samples. (a) $\text{Bi}_2\text{Te}_{2.7}\text{Se}_{0.3}$ -A; (b) $\text{Bi}_2\text{Te}_{2.7}\text{Se}_{0.3}$ -B; (c) $\text{Bi}_2\text{Te}_{2.55}\text{Se}_{0.45}$ -A; (d) $\text{Bi}_2\text{Te}_{2.55}\text{Se}_{0.45}$ -B; (e) $\text{Bi}_2\text{Te}_{2.4}\text{Se}_{0.6}$ -A; (f) $\text{Bi}_2\text{Te}_{2.4}\text{Se}_{0.6}$ -B.

The interatomic bonds in original clusters will be broken when the temperature reaches the critical scope. During this process, the original clusters are reduced, and new clusters with smaller size are formed. These changes impact solidification by inducing a much smaller critical nucleation radius, r^{*30} . In addition, since the solid-like clusters are destroyed during the TI-LLST process, the structural mismatch at the solid-liquid interface is exaggerated. Therefore, the solid-liquid interface energy (σ_{SL}) should be higher for B-group samples. According to the classical nucleation theory³⁷, the undercooling degree for nucleation, ΔT , can be expressed as:

$$\Delta T = \frac{2\sigma_{SL}V_S T_m}{\Delta H_m r^{*}} \quad (1)$$

where V_S is the molar volume of nucleation crystal, T_m is the melting point, and ΔH_m is the latent heat of fusion. Therefore, the ΔT will rise with σ_{SL} increasing and r^{*} decreasing, which is in good agreement with the lower nucleation temperature in B-group samples. The larger undercooling degree, higher nucleation rate, and higher fraction of nucleation sites will contribute to much finer solidification structures^{30, 37}.

As indicated by the cooling curves, the microstructures are expected to be refined in B-group samples. Therefore, optical microscopy, SEM, EBSD, and APT were utilized here to investigate the structural divergence for ingots solidified out of the liquid with different states (without and with experiencing TI-LLST). Figure 4 shows that the microstructures are mainly composed of alternative lamellae. The microstructures become finer and more homogenized in morphology for all B-group samples.

In order to characterize the possible phases and their compositions in the samples, XRD and EDS analysis were carried out on the surface parallel to the radial direction of solidified ingots. All XRD patterns (Fig. 5(b)) can be matched with the standard pattern of Bi_2Te_3 (JCPDS 15-0863, rhombohedral, $R\bar{3}m$, as shown in Fig. 5(a)) with only small deviations of the peak positions, which indicates that both phases, the bright and dark regions in Fig. 4, are solid solutions of Bi_2Te_3 . The EDS measurements were carried out to investigate the chemical composition of all six samples, shown in the Supplementary Figure S1 and Table S2. The results imply that the concentration between adjacent lamellae is slightly different. However, both XRD and EDS have a limited chemical and spatial resolution due to the penetration area, typically from few hundred nm to few μm . Therefore, APT analysis was performed to investigate the chemical and structural homogeneity in three dimensional space. APT is a destructive characterization technique based on the field evaporation theory. It is particularly effective at chemically and structurally characterizing materials in 3D at the nanometer scale^{38, 39}. We analysed two samples, $\text{Bi}_2\text{Te}_{2.55}\text{Se}_{0.45}$ -A and $\text{Bi}_2\text{Te}_{2.55}\text{Se}_{0.45}$ -B. Six APT tips were measured for each sample. Since the grain sizes of the measured samples are at the micrometre scale, while the APT tips are at the nanometre scale, it is rather difficult to get the grain boundary within the APT tips. Hence, only the single grain was analysed for sample $\text{Bi}_2\text{Te}_{2.55}\text{Se}_{0.45}$ -A, and the composition is very homogeneous in the grain interior (the results can be found in the Supplementary Information, Figure S2). Intriguingly, a very Te-rich phase was found in sample $\text{Bi}_2\text{Te}_{2.55}\text{Se}_{0.45}$ -B. According to the binary phase diagram of Bi-Te alloy¹⁰, the Te-rich phase is the eutectic phase. Figure 6(a) shows the 3D reconstruction of the volume analysed by APT. Mass spectra of the cylindrical regions of interest (ROIs) are shown in Fig. 6(b) and (c). The mass spectrum of the upper ROI shows that the peaks are mainly formed by Te and its isotopes, while the mass spectrum of the lower ROI shows very complex peaks formed by Bi, Te, Se, and their

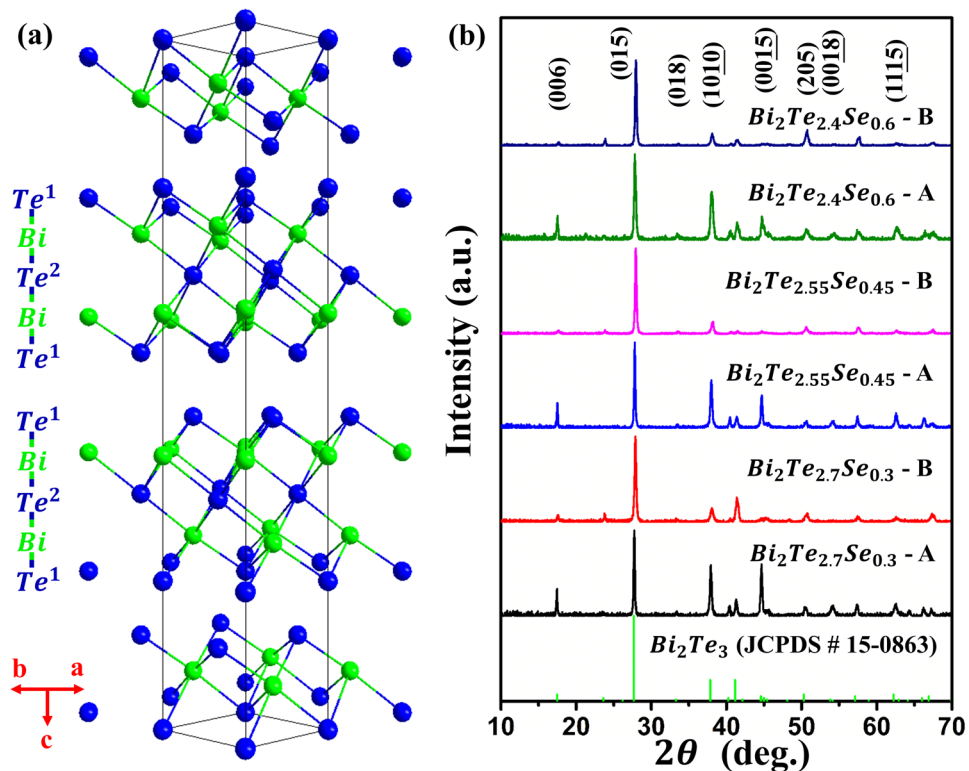


Figure 5. (a) Schematic diagram of the Bi_2Te_3 crystal structure; (b) XRD pattern of radial surfaces of as-cast $\text{Bi}_2\text{T}_{3-x}\text{Se}_x$ ($x = 0.3, 0.45, 0.6$) samples solidified from different liquid states.

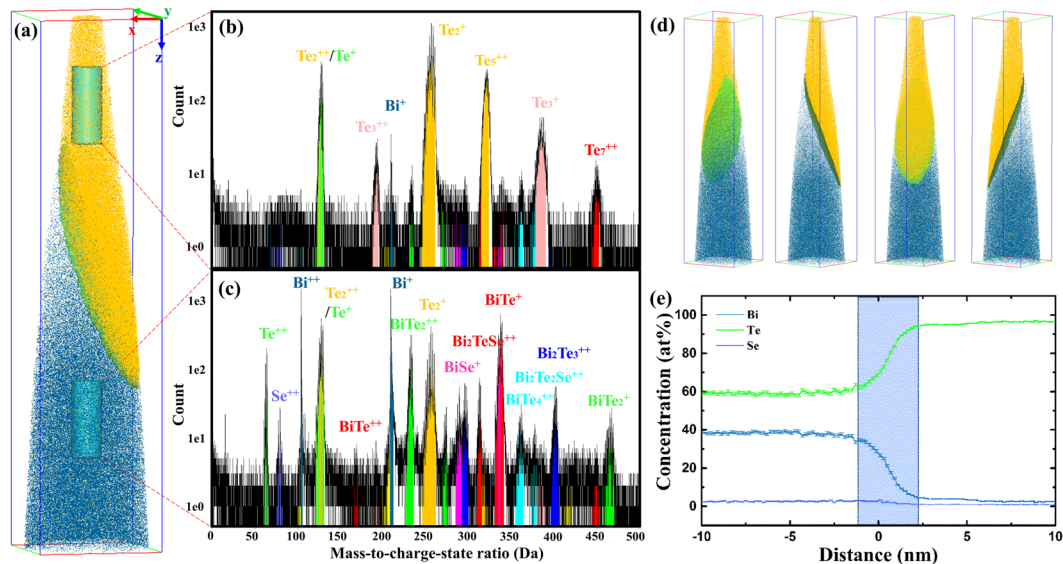


Figure 6. APT results of sample $\text{Bi}_2\text{Te}_{2.55}\text{Se}_{0.45}\text{-B}$. (a) Three-dimensional elemental maps showing the interface between a main-phase grain and a Te-rich grain (for clarity, only Te_5 and Bi ions are shown). The analysed volume is $80 \times 80 \times 350 \text{ nm}^3$; (b) mass spectrum of the cylindrical ROI from the upper part of the tip; (c) mass spectrum of the cylindrical ROI from the lower part of the tip; (d) different view directions showing the iso-concentration surface of 80 at% Te; (e) Proximity histogram (Proxigram) of the iso-surface of 80 at% Te. The shadow area depicts the diffusive area at the interface between the Te-rich phase and the matrix.

combinations. In order to analyse the composition evolution near the interface, an iso-concentration surface of 80 at% Te is created as highlighted by the green “leaf-like” plane. Figure 6(d) displays its shape from different viewing directions. The proximity histogram (proxigram), Fig. 6(e), is calculated based on the iso-surface of 80

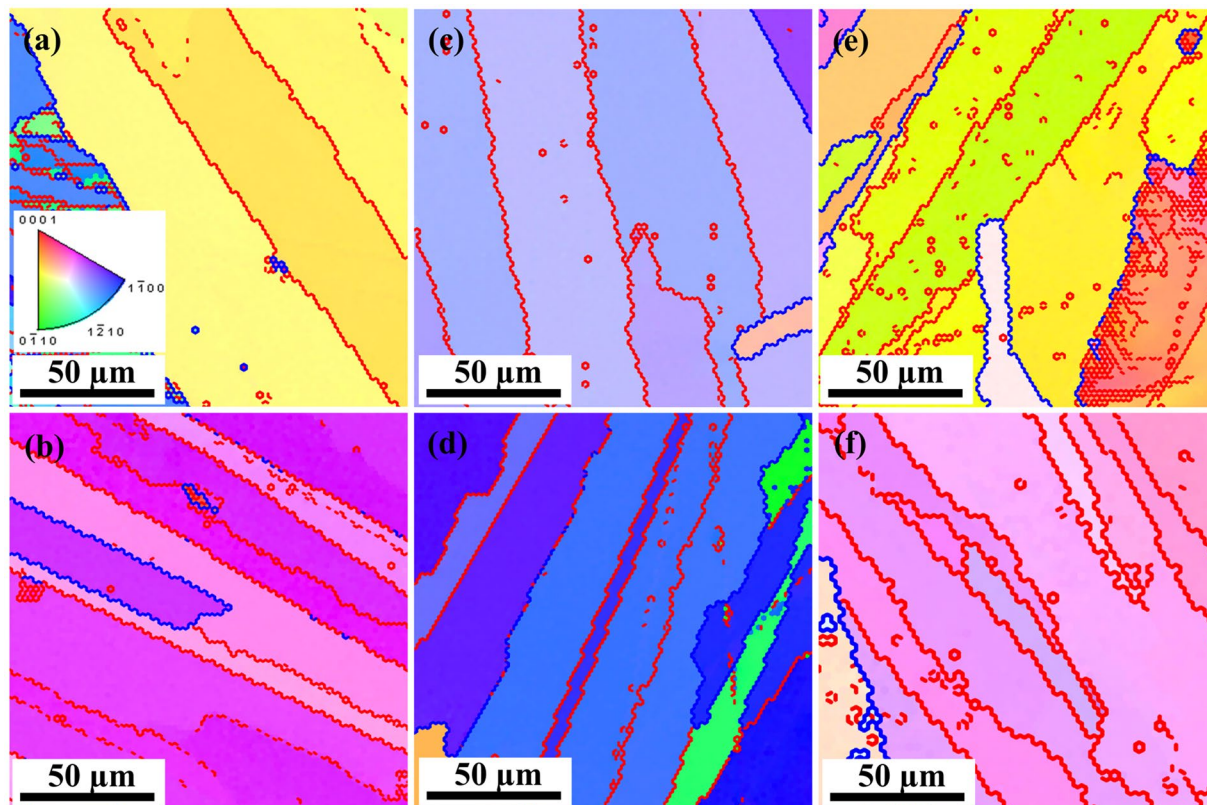


Figure 7. EBSD inverse pole figure maps covered with misorientation lines for grain boundaries. The red and blue lines represent the misorientation angles between $2^{\circ}\sim 15^{\circ}$ (LAGB) and $15^{\circ}\sim 180^{\circ}$ (high-angle GB), respectively. All the panels share the same legend of orientation map. (a) $\text{Bi}_2\text{Te}_{2.7}\text{Se}_{0.3}\text{-A}$; (b) $\text{Bi}_2\text{Te}_{2.7}\text{Se}_{0.3}\text{-B}$; (c) $\text{Bi}_2\text{Te}_{2.55}\text{Se}_{0.45}\text{-A}$; (d) $\text{Bi}_2\text{Te}_{2.55}\text{Se}_{0.45}\text{-B}$; (e) $\text{Bi}_2\text{Te}_{2.4}\text{Se}_{0.6}\text{-A}$; (f) $\text{Bi}_2\text{Te}_{2.4}\text{Se}_{0.6}\text{-B}$.

at% Te. The results of the proxigram clearly present the very Te-rich phase, which contains approximately 97 at% Te. The interface between the Te-rich phase and the matrix has a diffusive region with big variations of Te and Bi concentrations within ~ 3 nm, as highlighted by the shadow area in Fig. 6(e). This variation of composition will influence the local structural environment and carrier and phonon transport processes. No compositional fluctuation or precipitation was found in the interior of the matrix grain of sample $\text{Bi}_2\text{Te}_{2.55}\text{Se}_{0.45}\text{-B}$, consistent with the analysis of sample $\text{Bi}_2\text{Te}_{2.55}\text{Se}_{0.45}\text{-A}$. Since APT is a nanoscale characterization technique, we cannot give the conclusion that there is no Te-rich phase in sample $\text{Bi}_2\text{Te}_{2.55}\text{Se}_{0.45}\text{-A}$. However, from the viewpoint of solidification, we may conjecture that the Te-rich phase is more prone to form in B-group samples. The partition coefficient is defined as $k_0 = C_S^*/C_L^*$, where C_S^* and C_L^* are the concentrations of solute in the solid phase and liquid phase, respectively, at a specific solidification temperature. Given a nominal solute concentration C_0 , in the beginning of solidification, the concentration of solute in the solid phase is C_0k_0 . When $k_0 < 1$, the extra solute will be repelled out from the solid phase. Thus, the solute concentration in the liquid phase not far from the solid-liquid interface will increase and then reach C_0/k_0 . The smaller k_0 (for $k_0 < 1$) value, the larger difference of solute concentration at solid-liquid interface. The solidification partition coefficient (k_0) for Te in Bi-Te system is less than unity ($k_0 < 1$), thus Te will be rejected by the solid at the solid-liquid interface during the solidification process⁴⁰. Moreover, it is reported that the effective partition coefficient is decreased after experiencing TI-LLST⁴¹. The decrease of the partition coefficient leads to more Te being repelled from the solid-liquid interface. In addition, the pre-solidified matrix structures will form grooves between them, where the rejected Te is very easy to aggregate. With the enrichment of Te and decreasing of temperature, the eutectic reaction occurs at Te concentration of near 90 at% in the grooves. The eutectic structure is composed of pure Te and some small structures that have compositions similar to that of the matrix. APT data shows the composition of the eutectic Te is 97 at% because of the mutual diffusion between Te and Bi. The samples experienced TI-LLST have a higher nucleation rate and larger fraction of nuclei, leading to more solid-liquid interface. The eutectic reaction occurs at the Te-rich regions near the solid-liquid interface. Therefore, the increased solid-liquid interfaces increase the volume fraction of the Te-rich phase.

EBSD measurements were carried out to investigate the orientation relationship between two adjacent lamellae. As shown in Fig. 7, the misorientation angle between two adjacent lamellae is very often with values smaller than 15° , referring thus to low-angle grain boundaries (LAGBs). Normally, the LAGBs are composed of an array of dislocations⁴². These dislocations generate a strain field nearby, leading thus to a more pronounced phonon scattering at grain boundaries⁴³. Up to now, one of the highest thermoelectric figure-of-merit values of bulk Bi_2Te_3 -based material has been achieved by embedding dense dislocation arrays in grain boundaries⁴⁴. The

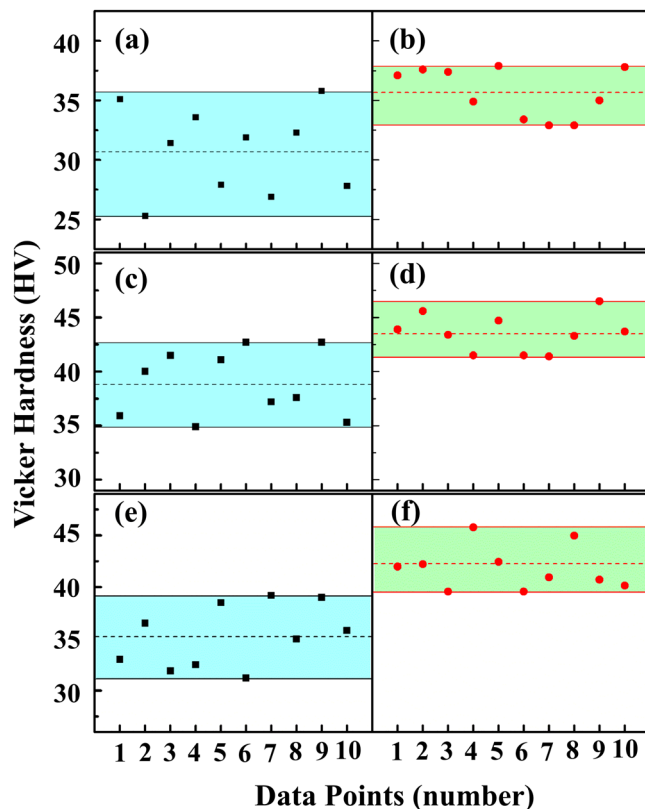


Figure 8. Vicker Hardness of all samples. The loading force and loading time are 0.245 N and 10 s, respectively. (a) $\text{Bi}_2\text{Te}_{2.7}\text{Se}_{0.3}$ -A; (b) $\text{Bi}_2\text{Te}_{2.7}\text{Se}_{0.3}$ -B; (c) $\text{Bi}_2\text{Te}_{2.55}\text{Se}_{0.45}$ -A; (d) $\text{Bi}_2\text{Te}_{2.55}\text{Se}_{0.45}$ -B; (e) $\text{Bi}_2\text{Te}_{2.4}\text{Se}_{0.6}$ -A; (f) $\text{Bi}_2\text{Te}_{2.4}\text{Se}_{0.6}$ -B.

(0001) pole figures also verify the strong preference for similar orientation of adjacent lamellae for all 6 samples, Supplementary Figure S3. It is found that electrons transport more easily in such textured structures, while the Seebeck coefficient is less influenced by the crystal orientation, and such structures are thus beneficial for higher electrical conductivity and thermoelectric power factor⁴⁵. Additionally, the small deviation in the composition of contiguous lamellae translates into a small degree of mass fluctuation at the boundary. This mass fluctuation can contribute to scattering of the heat-carrying phonons and may also serve as an energy barrier to filter out the low-energy carriers^{46, 47}. Thus, a high thermoelectric performance can be expected if these specular structures are rationally tailored, and the distinct solidification behaviours and microstructures from different liquid states supply an additional control over the structural modification.

Owing to the weak van der Waals force between $\text{Te}^{(1)} - \text{Te}^{(1)}$ layers, Fig. 5(a), the highly textured samples are vulnerable to fracture along this plane, largely restricting the working condition and service time of the thermoelectric devices, as well as wasting raw materials in cutting and other machining operations³. Therefore, more and more attention has been paid to improve the mechanical properties of Bi_2Te_3 -based materials in recent studies^{48–50}. As one example of TI-LLST influence on mechanical properties, the hardness was measured for all as-cast samples. Figure 8 demonstrates that the Vicker Hardness is enhanced and varies less for all B-group samples, which comes from the refined and homogenized microstructures solidified from the melt after experiencing TI-LLST. As with the less simple powder metallurgy and mechanical deformation methods^{48–50}, our free-solidification method with liquid state manipulation shows an ability to enhance the mechanical performance.

Conclusions

The abnormal humps on the ρ -T curves suggest that an irreversible TI-LLST occurs during the first heating process for all $\text{Bi}_2\text{Te}_{2.7}\text{Se}_{0.3}$, $\text{Bi}_2\text{Te}_{2.55}\text{Se}_{0.45}$, and $\text{Bi}_2\text{Te}_{2.4}\text{Se}_{0.6}$ liquid alloys in temperature ranges of 790.6–900.4 °C, 810.1–940.5 °C, and 800.7–920.6 °C, respectively. It is assumed that the structural transition results from the dissolution of short-range ordered Bi_2Te_3 , Bi_2Se_3 , and Bi-Te-Se ternary clusters. Based on this information, the samples solidified out of the liquids with TI-LLST exhibit significantly different solidification behaviours: the solidification undercooling degree is increased; the nucleation rate is enhanced; the crystal growth time is shortened. These changes lead to refinement of solidification microstructures, an increased prevalence of low-angle grain boundaries, and enhancement of Vicker Hardness. The Te-rich eutectic phase was observed by the state-of-the-art APT technique. The composition evolution near the matrix-Te phase boundary at the nanometre scale also was analysed, which may help to better understand the carrier transport process at the interface. It is reasonable to conjecture that these structural alterations might lead to an enhancement of the thermoelectric and mechanical properties of commercial-scale ingots, thus benefitting applications.

References

- Vining, C. B. Semiconductors are cool. *Nature* **413**, 577–578, doi:10.1038/35098159 (2001).
- Bell, L. E. Cooling, Heating, generating power, and recovering waste heat with thermoelectric systems. *Science* **321**, 1457–1461, doi:10.1126/science.1158899 (2008).
- Goldsmid, H. B. T. Its Alloys as Materials for Thermoelectric Generation. *Materials* **7**, 2577–2592, doi:10.3390/ma7042577 (2014).
- Snyder, G. J. & Toberer, E. S. Complex thermoelectric materials. *Nat. Mater.* **7**, 9–114, doi:10.1038/nmat2090 (2008).
- Zhu, M. *et al.* One order of magnitude faster phase change at reduced power in Ti-Sb-Te. *Nat. Commun.* **5**, 4086, doi:10.1038/ncomms5086 (2014).
- Zhang, H. *et al.* Topological insulators in Bi₂Se₃, Bi₂Te₃, and Sb₂Te₃ with a single Dirac cone on the surface. *Nat. Phys* **5**, 438–442, doi:10.1038/nphys1270 (2009).
- Liu, D. *et al.* Anisotropic n-Type Bi₂Te₃-In₂Te₃ Thermoelectric Material Produced by Seeding Zone Melting and Solid State Transformation. *Cryst. Growth Des.* **16**, 617–624, doi:10.1021/acs.cgd.5b01015 (2016).
- Laopaiboon, J. *et al.* Competing anisotropic microstructures of Bi₂(Te_{0.95}Se_{0.05})₃ thermoelectric materials by Bridgman technique. *Mater. Lett.* **141**, 307–310, doi:10.1016/j.matlet.2014.11.124 (2015).
- Ivanova, L. & Granatkina, Y. V. Thermoelectric properties of Bi₂Te₃-Sb₂Te₃ single crystals in the range 100–700 K. *Inorg. Mater* **36**, 672–677, doi:10.1007/BF02758419 (2000).
- Rowe, D. M. *CRC handbook of thermoelectrics* (CRC press, 1995).
- Poudel, B. *et al.* High-thermoelectric performance of nanostructured bismuth antimony telluride bulk alloys. *Science* **320**, 634–638, doi:10.1126/science.1156446 (2008).
- Cai, X. *et al.* Improved thermoelectric properties of Bi₂Te_{3-x}Se_x alloys by melt spinning and resistance pressing sintering. *J. Phys. D: Appl. Phys* **47**, 115101, doi:10.1088/0022-3727/47/11/115101 (2014).
- Hu, L. *et al.* Tuning Multiscale Microstructures to Enhance Thermoelectric Performance of n-Type Bismuth-Telluride-Based Solid Solutions. *Adv. Energy Mater* **5**, 1500411, doi:10.1002/aenm.201500411 (2015).
- Guo, X. *et al.* Thermoelectric transport properties and crystal growth of BiSbTe₃ bulk materials produced by a unique high-pressure synthesis. *CrystEngComm* **15**, 7236, doi:10.1039/c3ce40780b (2013).
- Yu, Y. *et al.* Enhancing the thermoelectric performance of free solidified p-type Bi_{0.5}Sb_{1.5}Te₃ alloy by manipulating its parent liquid state. *Intermetallics* **66**, 40–47, doi:10.1016/j.intermet.2015.06.020 (2015).
- Yu, Y. *et al.* Influence of melt overheating treatment on solidification behavior of BiTe-based alloys at different cooling rates. *Mater. Des* **88**, 743–750, doi:10.1016/j.matdes.2015.09.074 (2015).
- Li, M., Zhang, Y., Wu, C. & Geng, H. Effect of liquid-liquid structure transition on solidification of Sn₅₇Bi₄₃ alloy. *Appl. Phys. A* **122**, doi: 10.1007/s00339-016-9723-5 (2016).
- Qiu, D., Zhang, M.-X., Taylor, J., Fu, H.-M. & Kelly, P. A novel approach to the mechanism for the grain refining effect of melt superheating of Mg–Al alloys. *Acta Mater.* **55**, 1863–1871, doi:10.1016/j.actamat.2006.10.047 (2007).
- Katayama, Y. *et al.* A first-order liquid-liquid phase transition in phosphorus. *Nature* **403**, 170–173, doi:10.1038/35003143 (2000).
- Zu, F. Q. *et al.* Observation of an anomalous discontinuous liquid-structure change with temperature. *Phys. Rev. Lett.* **89**, 125505, doi:10.1103/PhysRevLett.89.125505 (2002).
- Kresse, G. & Hafner, J. Ab initio molecular dynamics for liquid metals. *Phys. Rev. B* **47**, 558–561, doi:10.1103/PhysRevB.47.558 (1993).
- Zu, F., Zhu, Z., Zhang, B., Feng, Y. & Shui, J. Post-melting anomaly of Pb-Bi alloys observed by internal friction technique. *J. Phys.: Condens. Matter* **13**, 11435, doi:10.1088/0953-8984/13/50/303 (2001).
- Zu, F., Ding, G. & Li, X. Change in solidification behavior of Bi–Sb₁₀ alloy after liquid structural transition. *J. Cryst. Growth* **310**, 397–403, doi:10.1016/j.jcrysgro.2007.10.031 (2008).
- Iida, T. & Guthrie, R. I. *The physical properties of liquid metals* (Clarendon Press, Oxford, 1988).
- Zu, F. Temperature-Induced Liquid-Liquid Transition in Metallic Melts: A Brief Review on the New Physical Phenomenon. *Metals* **5**, 395–417, doi:10.3390/met5010395 (2015).
- Li, X. F., Zu, F. Q., Liu, L. J., Yu, J. & Zhou, B. Hump phenomenon on resistivity-temperature curve in liquid Bi, Sb and their alloys. *Phys. Chem. Liq.* **45**, 531–539, doi:10.1080/00319100701344594 (2007).
- Greenberg, Y. *et al.* Evidence for a temperature-driven structural transformation in liquid bismuth. *EPL (Europhys. Lett.)* **86**, 36004, doi:10.1209/0295-5075/86/36004 (2009).
- Hafner, J. & Philipp, A. Low-temperature electrical resistivity of amorphous Ca-Mg alloys. *J. Phys. F: Metal Phys* **14**, 1685–1691, doi:10.1088/0305-4608/14/7/016 (1984).
- Cruz, H., Gonzalez, C., Juárez, A., Herrera, M. & Juárez, J. Quantification of the microconstituents formed during solidification by the Newton thermal analysis method. *J. Mater. Process. Technol.* **178**, 128–134, doi:10.1016/j.jmatprotec.2006.03.152 (2006).
- Kurz, W. & Fisher, D. J. *Fundamentals of solidification* (1986).
- Poole, P. H., Grande, T., Angell, C. A. & McMillan, P. F. Polymorphic Phase Transitions in Liquids and Glasses. *Science* **275**, 322–323, doi:10.1126/science.275.5298.322 (1997).
- McMillan, P. Phase transitions: Jumping between liquid states. *Nature* **403**, 151–152, doi:10.1038/35003088 (2000).
- Kurita, R. & Tanaka, H. Critical-Like Phenomena Associated with Liquid-Liquid Transition in a Molecular Liquid. *Science* **306**, 845–848, doi:10.1126/science.1103073 (2004).
- Mudry, S. The structure of liquid Bi₂Te₃ alloys near the stoichiometric region. *J. Alloys Compd.* **267**, 100–104, doi:10.1016/S0925-8388(97)00526-4 (1998).
- Kakinuma, F., Fukunaga, T., Misawa, M. & Suzuki, K. Neutron diffraction study of liquid Bi-Se alloys. *J. Non-Cryst. Solids* **156**, 76–79, doi:10.1016/0022-3093(93)90133-I (1993).
- Usuki, T., Shirakawa, Y., Tamaki, S. & Takeda, S. I. Neutron Diffraction Study of Liquid Bi–Se Alloys. *J. Phys. Soc. Jpn.* **62**, 148–154, doi:10.1143/JPSJ.62.148 (1993).
- Turnbull, D. Formation of Crystal Nuclei in Liquid Metals. *J. Appl. Phys.* **21**, 1022–1028, doi:10.1063/1.1699435 (1950).
- Zhou, X., Yu, X. X., Kaub, T., Martens, R. L. & Thompson, G. B. Grain Boundary Specific Segregation in Nanocrystalline Fe(Cr). *Sci. Rep* **6**, 34642, doi:10.1038/srep34642 (2016).
- Yamini, A., Li, T., Mitchell, D. R. G. & Cairney, J. M. Elemental distributions within multiphase quaternary Pb chalcogenide thermoelectric materials determined through three-dimensional atom probe tomography. *Nano Energy* **26**, 157–163, doi:10.1016/j.nanoen.2016.05.019 (2016).
- Cosgrove, G. J., McHugh, J. P. & Tiller, W. A. Effect of Freezing Conditions on the Thermoelectric Properties of BiSbTe₃ Crystals. *J. Appl. Phys.* **32**, 621–623, doi:10.1063/1.1736059 (1961).
- Zu, F. Q., Chen, J., Li, X. F., Mao, L. N. & Liu, Y. C. A new viewpoint to the mechanism for the effects of melt overheating on solidification of Pb-Bi alloys. *J. Mater. Res.* **24**, 2378–2384, doi:10.1557/jmr.2009.0294 (2011).
- Callister, W. D. & Rethwisch, D. G. *Materials science and engineering: an introduction* Vol. 7 (Wiley New York, 2007).
- Kim, H.-S., Kang, S. D., Tang, Y., Hanus, R. & Jeffrey Snyder, G. Dislocation strain as the mechanism of phonon scattering at grain boundaries. *Mater. Horiz* **3**, 234–240, doi:10.1039/c5mh00299k (2016).
- Kim, S. I. *et al.* Dense dislocation arrays embedded in grain boundaries for high-performance bulk thermoelectrics. *Science* **348**, 109–114, doi:10.1126/science.aaa4166 (2015).

45. Hu, L. P. *et al.* Improving thermoelectric properties of n-type bismuth–telluride-based alloys by deformation-induced lattice defects and texture enhancement. *Acta Mater.* **60**, 4431–4437, doi:10.1016/j.actamat.2012.05.008 (2012).
46. Jo, S. *et al.* Simultaneous improvement in electrical and thermal properties of interface-engineered BiSbTe nanostructured thermoelectric materials. *J. Alloys Compd.* **689**, 899–907, doi:10.1016/j.jallcom.2016.08.033 (2016).
47. Li, J. *et al.* BiSbTe-Based Nanocomposites with HighZT: The Effect of SiC Nanodispersion on Thermoelectric Properties. *Adv. Funct. Mater.* **23**, 4317–4323, doi:10.1002/adfm.201300146 (2013).
48. Zheng, Y. *et al.* Mechanically Robust BiSbTe Alloys with Superior Thermoelectric Performance: A Case Study of Stable Hierarchical Nanostructured Thermoelectric Materials. *Adv. Energy Mater.* **5**, 1401391, doi:10.1002/aenm.201401391 (2015).
49. Zheng, Y. *et al.* High-Temperature Mechanical and Thermoelectric Properties of p-Type Bi_{0.5}Sb_{1.5}Te₃ Commercial Zone Melting Ingots. *J. Electron. Mater.* **43**, 2017–2022, doi:10.1007/s11664-013-2938-8 (2013).
50. Simard, J.-M., Vasilevskiy, D. & Turenne, S. In *Thermoelectrics, 2003 Twenty-Second International Conference on-ICT* 13–18 (IEEE).

Acknowledgements

This research is supported by the National Natural Science Foundation of China (grants No. 51371073), the China Postdoctoral Science Foundation (grants No. 2013M531502) and the National Basic Research Program of China (973 Program) (grant No. 2012CB825702). Yuan Yu acknowledges the Chinese Scholarship Council for providing his visiting scholar stipend.

Author Contributions

F.Q.Z. conceived and supervised this study. Y.Y. carried out the EDS and EBSD experiments. Z.W. and Y.Y. carried out the liquid resistivity and the solidification experiments. Y.Y. and O.M. carried out the APT measurements. Z.Y.H., B.Z., X.Y.W., and N.G. carried out the XRD and Vicker Hardness measurements. Y.Y, Z.Y.H., and Z.W. analysed all the data. Y.Y, O.C.M., Z.Y.H., and F.Q.Z. wrote the manuscript. All authors have reviewed, discussed, and approved the results and conclusions of this manuscript.

Additional Information

Supplementary information accompanies this paper at doi:10.1038/s41598-017-02507-4

Competing Interests: The authors declare that they have no competing interests.

Publisher's note: Springer Nature remains neutral with regard to jurisdictional claims in published maps and institutional affiliations.



Open Access This article is licensed under a Creative Commons Attribution 4.0 International License, which permits use, sharing, adaptation, distribution and reproduction in any medium or format, as long as you give appropriate credit to the original author(s) and the source, provide a link to the Creative Commons license, and indicate if changes were made. The images or other third party material in this article are included in the article's Creative Commons license, unless indicated otherwise in a credit line to the material. If material is not included in the article's Creative Commons license and your intended use is not permitted by statutory regulation or exceeds the permitted use, you will need to obtain permission directly from the copyright holder. To view a copy of this license, visit <http://creativecommons.org/licenses/by/4.0/>.

© The Author(s) 2017